Express Polymer Letters Vol.18, No.4 (2024) 349–358
Available online at www.expresspolymlett.com
https://doi.org/10.3144/expresspolymlett.2024.26

Research article

3D printing of porous poly(ε-caprolactone)-poly(trimethylene carbonate)-poly(ε-caprolactone) triblock copolymers and nano-apatite composite structures

Aysun Güney[1], *Lena Kernebeck*[1,2], *Dirk W. Grijpma*[1*]

[1]TechMed Centre, and Faculty of Science and Technology, Department of Advanced Organ Bioengineering and Therapeutics, University of Twente, PO Box 271, 7500 AE Enschede, The Netherlands
[2]Current address: Phytowelt GreenTechnologies GmbH, Nattermannallee 1, 50829 Köln, Germany

Received 15 September 2023; accepted in revised form 14 December 2023

Abstract. Biodegradable porous poly(ε-caprolactone)-poly(trimethylene carbonate)-poly(ε-caprolactone) triblock copolymers (PCL-*b*-PTMC-*b*-PCL) were synthesized by sequentɛial polymerization of trimethylene carbonate (TMC) and ε-caprolactone (CL), and novel composites of PCL-*b*-PTMC-*b*-PCL with different amounts of nano-apatite (nAp) were prepared. This PTMC-based polymer matrix, which does not degrade into acidic compounds, together with the nanometer-sized apatite, which influences cell behavior, is an ideal bone regenerative material.
Solvent casting these composites from chloroform solutions yielded solid films with excellent handling properties. The *E*-modulus of the nano-composite materials increases with nAp content, while toughness, tensile strength and elongation at break decrease.
Using EC as solvent, porous composite films of PCL-*b*-PTMC-*b*-PCL and nAp could readily be prepared.
The composites in EC were processed into form-stable designed tissue engineering scaffolds by 3D printing at relatively mild conditions. Besides the pore network structure with pores of 530 to 620 µm which corresponded to the design, smaller pores of 5–30 µm (due to EC crystallization) and even smaller ones of 200–500 nm (resulting from liquid-liquid exchange upon extraction of the solvent in the polymer rich phase) were observed in the printed composite scaffolds.

Keywords: *biomedical polymer, ring-opening polymerization, nanocomposites, additive manufacturing, scaffold*

1. Introduction

Extrusion-based additive manufacturing processes (3D printing) have emerged as an appealing tool in the fabrication of designed and patient-specific tissue engineering scaffolds [1]. For any type of tissue, only an open and interconnected network of pores allows mass transport of oxygen, nutrients and metabolic waste products, thereby promoting vascularization and cell viability [2–4]. Despite the many benefits, 3D printing in biomedical engineering is hindered by the limited availability of suitable materials that can be printed [5, 6].

Natural bone is a complex, highly organized hierarchical structure from the nano- to the macro-scale. It can be considered a composite material mainly consisting of organic collagen fibrils and inorganic (carbonated) hydroxyapatite nanocrystals embedded within them, and has excellent mechanical properties. It is composed of two main bone tissue types: cortical (or compact) bone, which is dense and has 5–10% porosity with pores of 10–50 µm diameter, and cancellous (or trabecular) bone, which is highly porous (75–85% porosity) with 300–600 µm diameter interconnected open pores [7, 8].

*Corresponding author, e-mail: d.w.grijpma@utwente.nl

Besides the obvious mechanical properties, bone tissues play important biological roles, too. They contain a variety of cells, such as osteocytes, osteoblasts, osteoclasts and undifferentiated osteogenic cells, which maintain bone homeostasis. Furthermore, cancellous bone is highly vascularized and innervated, and haematopoiesis takes place in the bone marrow in cancellous bone [9, 10].

In bone tissue engineering, scaffolds with an interconnected porosity have been prepared with pores of different sizes that allow for vascularization of the cell construct as well as the formation of bone tissue [11–14], and it is of great interest to make use of porous structures prepared from bone-forming materials [14]. Composites of bone-inducing or bone-conducting calcium phosphates (*e.g.* hydroxyapatite, nano-apatite, and tricalcium phosphate) and synthetic biodegradable polymers have been previously used to prepare such scaffolding structures by 3D printing [14–17]. We have shown that *in vivo*, composites based on calcium phosphates and a biodegradable poly(trimethylene carbonate) (PTMC) matrix, which degrades by a surface erosion process without the formation of acidic degradation products, have excellent bone-forming characteristics [17–19].

Previously, we reported on the synthesis and properties of triblock copolymers prepared from 1,3-trimethylene carbonate and ε-caprolactone [20]. These PCL-*b*-PTMC-*b*-PCL block copolymers consist of an amorphous poly(trimethylene carbonate) segment (T_g is approximately –17 °C) and two crystallizable poly(ε-caprolactone) segments (T_g and T_m are respectively approximately–60 and 65 °C). The crystallizability of the poly(ε-caprolactone) segments allows these PTMC-based triblock copolymers to be processed by an extrusion-based 3D printing process. In this current paper, we describe the preparation and properties of PCL-*b*-PTMC-*b*-PCL and nano-apatite (nAp) composites. The size of the inorganic component in natural bone is considered to be important not only for the mechanical properties of bone, but also for enhanced protein adsorption and osteoblast adhesion. Therefore, in a bone regenerative implant material, an artificial matrix incorporating nanometer-sized apatite can be expected to have an influence on the behavior of cells [22–25]. We have processed these composites into well-defined designed porous structures by 3D printing using EC as a benign crystallizable solvent. We expect these porous composite structures to be highly suited for bone tissue engineering.

2. Experimental

2.1. Materials

1,3-trimethylene carbonate (TMC) was obtained from Huizhou ForYou Medical Devices Company (Huizhou, China), diphenyl phosphate (DPP) from Tokyo Chemical Industry UK Ltd. (Oxford, UK), and 2,2-dimethyl-1,3-propanediol (DMP) from Sigma-Aldrich (Taufkirchen, Germany). ε-caprolactone (ε-CL), obtained from Acros Organics (Geel, Belgium), was purified by drying over CaH_2 and distillation under vacuum. Nano-apatite (nAp) aggregates (ø = 15 μm) of needle-like apatite crystals of 200 to 400 nm long and 20 to 50 nm wide were kindly provided by XPand Biotechnology BV (Amsterdam, The Netherlands). Ethylene carbonate (EC) and chloroform were obtained from Sigma-Aldrich (Taufkirchen, Germany) and used as received. Dichloromethane and methanol, respectively obtained from VWR Chemicals and Merck (Schiphol-Rijk, The Netherlands), were of analytical grade and used as received.

2.2. Synthesis of the PCL-*b*-PTMC-*b*-PCL triblock copolymer

The PCL-*b*-PTMC-*b*-PCL triblock copolymer was synthesized by sequential ring-opening polymerization (ROP) of TMC and ε-CL. As reported before [20], TMC and DMP were charged in a flask under an argon atmosphere using DPP as a catalyst. The molar ratio of DPP catalyst to DMP initiator was 1:1. Under an argon atmosphere, a hydroxy-terminated PTMC oligomer was first prepared by polymerization for 72 h at a temperature of 70 °C. Subsequently, this PTMC oligomer was used to initiate the ROP of ε-CL. This reaction was allowed to proceed for another 24 h under the same conditions, leading to the formation of a PCL-*b*-PTMC-*b*-PCL triblock copolymer. The targeted molar masses of the PTMC- and PCL blocks were, respectively 40 and 20 kg/mol.

The obtained polymers were analysed by ^{1}H-nuclear magnetic resonance (NMR) with a 400 MHz Bruker Ascend (San Jose,USA) instrument, using deuterated chloroform (Sigma-Aldrich) as solvent.

The thermal characteristics of the polymer were evaluated by differential scanning calorimetry (DSC). The polymer was heated from –100 to 100 °C at a rate of 10 °C/min, after 1 min, it was then cooled to

–100°C at 20 °C/min, after which a second scan was taken at 10 °C/min. This erases the thermal history of the specimens. The glass transition (T_g) and the melting (T_m) temperatures were obtained in the second heating scan.

2.3. Preparation of PCL-*b*-PTMC-*b*-PCL and nAp composites

A series of PCL-*b*-PTMC-*b*-PCL and nAp composites were prepared by first dispersing the nAp nanoparticles in chloroform by stirring and use of ultrasound, then dissolving the PCL-*b*-PTMC-*b*-PCL polymer in this dispersion at a concentration of 0.1 g/mL at ambient conditions by overnight stirring. Finally, the dispersions were precipitated in cold methanol and dried in a vacuum oven for 7 days. Composites containing 0, 20 and 40 wt% nAp were prepared, these are indicated as n0 (nAp:PCL-*b*-PTMC-*b*-PCL = 0:100), n20 (nAp:PCL-*b*-PTMC-*b*-PCL = 20:80), and n40 (nAp:PCL-*b*-PTMC-*b*-PLC 40:60).

The nAp content in the composites was verified by thermogravimetric analysis using a TGA7 (Perkin Elmer, Waltham, USA). Samples (5–10 mg) were heated under a nitrogen flow from 30 to 600 °C at a heating rate of 20 °C/min.

2.4. Preparation and characterization of non-porous and porous PCL-*b*-PTMC-*b*-PCL and nAp composite films

Non-porous and porous films were prepared by casting solutions on glass plates. The solutions for preparing non-porous films were made by dissolving the dried precipitate in chloroform at a concentration of 0.3 g/mL for 1 day. After casting and drying at ambient conditions for 7 days, the thickness of the obtained films was 150 to 200 μm. All chloroform had evaporated. For the fabrication of porous (composite) films, the dried precipitates were redissolved in EC at 50°C at a concentration of 25 wt% for 1 day, sonicated for 15 min, and cast on glass plates before use. They were then continuously extracted for 2 days in cold demi water (4 °C) and dried at ambient conditions, yielding 200 to 250 μm thick films.

For tensile testing, ASTM D882-91 tensile test specimens (100×5 mm) were punched out from the non-porous and porous films. A universal tensile tester (Zwick Z020, Ulm, Germany) equipped with a 500 N load cell was used. The distance between the clamps was 50 mm, and the crosshead speed was 50 mm/min. The tensile tests were conducted in five-fold.

The morphology of the pore network of the porous films was analysed by high-resolution scanning electron microscopy (HR-SEM, Zeiss 1550, Oberkochen, Germany) after sputter-coating with gold. Characteristics of the pores were determined from the images using ImageJ software (https://imagej.nih.gov/) [21].

2.5. 3D printing of composite scaffolds

Cylindrical scaffolds were designed using Solidworks 3D computer-aided design (CAD) software (www.solidworks.com). Figure 1 shows the scaffold design. The scaffold design was imported into Repetier-Host software (www.repetier.com) to perform the slicing into layers and produce the G-code for the 3D printer.

The scaffolds were fabricated by 3D printing using a pneumatic extrusion-based 3D (bio)printer (Biobots1, Louisville, KY, USA). The apparatus is equipped

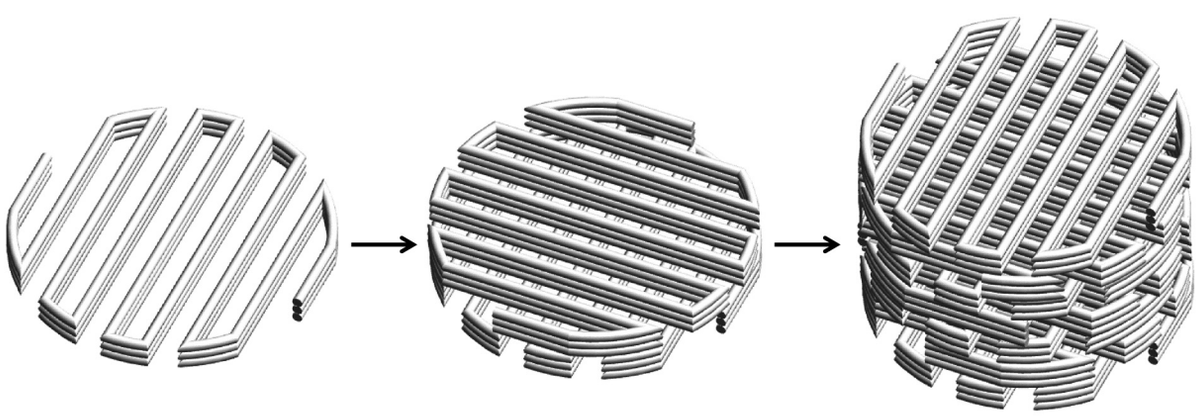

Figure 1. Design of the cylindrical scaffolds (diameter 6 mm, height 4.2 mm) that are to be prepared by 3D printing. The lay-down pattern of the fibres is such that after depositing three layers, the pattern is rotated 90°. A total of 21 layers are to be deposited.

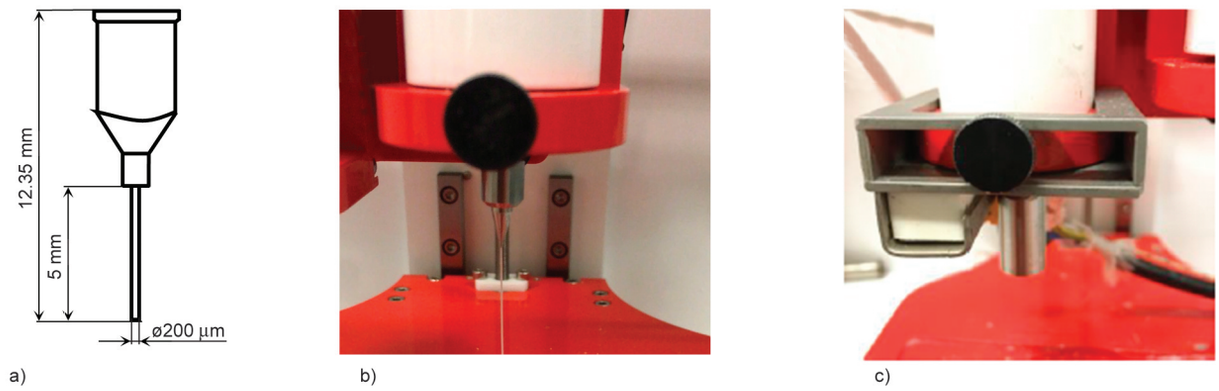

Figure 2. a) Characteristics of the stainless steel extrusion nozzle used in the 3D printing process. The tip length of the nozzle is 12.7 mm, and the inner diameter is 200 µm. b) Extrusion nozzle mounted onto the syringe, and c) heating element fitted to the extrusion nozzle.

with a heated 10 mL stainless steel syringe with a diameter of 14.7 mm and fitted with a stainless steel extrusion nozzle (PVA, Helmond, The Netherlands), see Figure 2a. To heat the mounted extrusion nozzle (Figure 2b), an in-house built heating element (Figure 2c) was used.

The precipitated n0, n20 and n40 composites were dissolved in EC at 50 °C at a concentration of 25 wt% and charged into the heated metal syringe. The thermal behavior of these composite solutions was also assessed by DSC, allowing optimization of the printing conditions. Suitable conditions were found to be: a cylinder temperature of 65–70 °C and an extrusion nozzle temperature of 70 °C. After 1 h equilibration period, the solutions were extruded at a pressure of 450 to 650 kPa and a printing speed of 8 mm/s in the x-y direction. Upon extrusion of a layer, the structure was cooled with dry ice to ensure solidification by crystallization of EC. A next layer could then be printed onto the previous layer. The printed scaffolds were then extracted for 2 days in cold demineralized water (4 °C) and dried at ambient conditions.

Light microscopy (Leica DMRX optical microscope and Leica MZ 125 stereo microscope, Leica, Wetzlar, Germany) and SEM analysis (1550 HR-SEM, Zeiss, Germany) were used to evaluate the structure and morphology of the 3D printed scaffolds.

3. Results and discussion

3.1. Properties of the PCL-*b*-PTMC-*b*-PCL triblock copolymer

The PCL-*b*-PTMC-*b*-PCL triblock copolymer was obtained by sequential polymerization of TMC and ε-CL [20]. Figure 3 illustrates the reaction steps involved.

The TMC monomer conversion in the first step was determined from the integral values of the characteristic *–CO–O–C**H**$_2$–CH$_2$–CH$_2$–O–* peaks of TMC (at 4.44 to 4.48 ppm) and the integral value of the corresponding peaks of PTMC at 4.18 to 4.32 ppm in the NMR spectra. M_n of the precursor PTMC polymer was determined by comparison of the integral value of the methyl H atoms of the DMP component at 0.94 ppm with those of the PTMC peaks at 4.18 to 4.32 ppm.

The conversion of ε-CL in the second reaction step was determined by comparison of the integral values of the characteristic *–O–CH$_2$–CH$_2$–CH$_2$–CH$_2$– C**H**$_2$––CO–O–* peaks of ε-CL monomer at 2.52 to 2.67 ppm which can be distinguished from those of the corresponding polymeric peaks of PCL at 2.27 to 2.34 ppm.

The composition of the purified PCL-*b*-PTMC-*b*-PCL triblock copolymer was calculated from the ratios of the integral values of the peak signals at 2.01 to 2.09 ppm or at 4.18 to 4.32 ppm (corresponding to the PTMC block) and at 2.26 to 2.33 ppm (corresponding to the PCL blocks). Knowing the M_n of the PTMC block and the composition of the copolymer, the M_n of the triblock copolymers can readily be calculated as well.

The TMC monomer conversion was 99.5%, while the number-averaged molecular weight (M_n) of the PTMC block was found to be 38 kg/mol. In the subsequent ε-CL polymerization, the ε-CL conversion was 99.0%. M_n of the PCL blocks of the triblock-copolymer was 19.5 kg/mol, and the overall M_n of the triblock-copolymer was 77 kg/mol. These values are close to our targeted values.

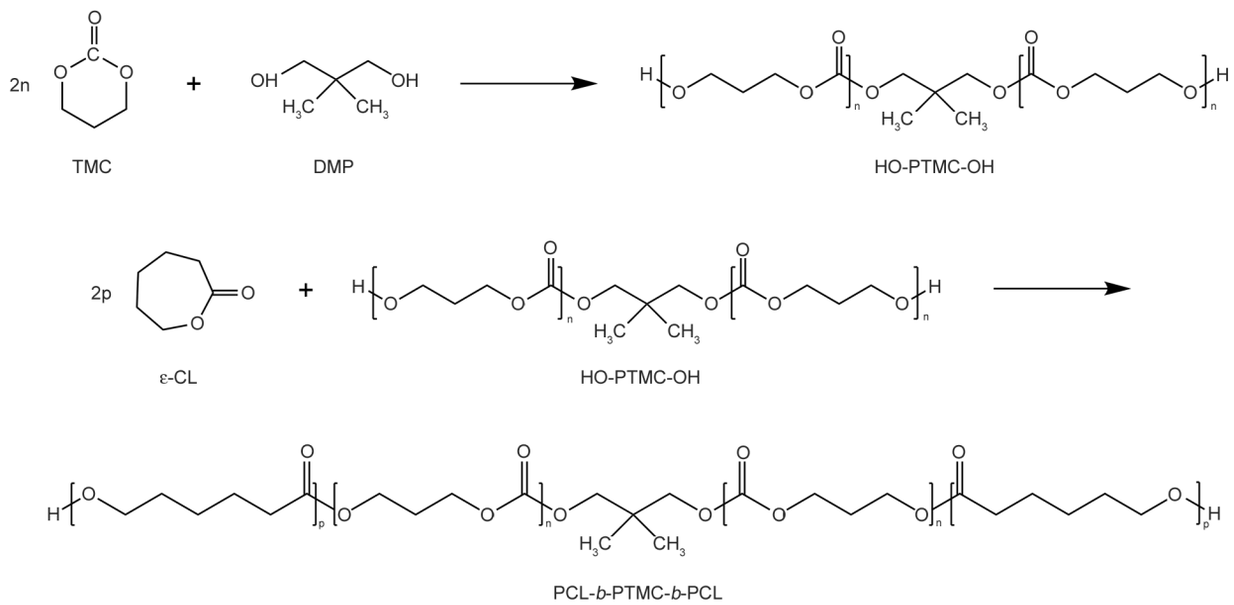

Figure 3. Reaction scheme illustrating the synthesis of PCL-*b*-PTMC-*b*-PCL triblock copolymers. In the first reaction step, ring-opening polymerization of the TMC monomer with bifunctional DMP as initiator yields an α-ω hydroxy group-terminated PTMC block. Upon addition of ε-CL monomer and subsequent polymerization, a PCL-*b*-PTMC-*b*-PCL triblock copolymer is formed in the second step.

3.2. Thermal- and mechanical properties of PCL-*b*-PTMC-*b*-PCL and nAp composites

DSC analysis showed that the PCL-*b*-PTMC-*b*-PCL triblock copolymer had a segmented, phase-separated structure with two glass transition temperatures and a single melting temperature. T_{g1} and T_m corresponding to the PCL segments were respectively –60 and 55 °C, while T_{g2} corresponding to the non-crystallizable PTMC segment was –20 °C.

Thermogravimetric analysis was used to determine the nAp contents in the different PCL-*b*-PTMC-*b*-PCL and nAp composites. While the polymeric component decomposes at temperatures between approximately 325 and 425 °C, the ceramic component remains unchanged at temperatures up to 600 °C. It was determined that the n0, n20, and n40 composites contained respectively 0, 19 and 35 wt% nAp after precipitation and drying.

To investigate the mechanical properties of the n0, n20, and n40 PCL-*b*-PTMC-*b*-PCL and nAp composites, the cast non-porous films were subjected to tensile testing. In Table 1, an overview of their mechanical properties is given. It can be seen that with an increase in nAp content, the elasticity modulus (E) of the composites significantly increases. While the yield stress does not change very much, the tensile stress at break, the elongation at break and the toughness (energy to break, area under the stress-strain curve) decrease considerably.

For the porous films prepared by casting solutions in ethylene carbonate and subsequent extraction with water and drying, the porosity is close to values that could be expected based on the total solids content in the solutions (25 wt%). The dimensions of the pores ranged from 20–31 in µm length and 11–16 µm in width.

Table 1. Tensile properties of non-porous and porous PCL-*b*-PTMC-*b*-PCL and nAp composite films. (n = 5, average ±SD).

	Specimen	Porosity [%]	E [MPa]	σ_{yield} [MPa]	ε_{yield} [%]	σ_{break} [MPa]	ε_{break} [%]	Toughness [N/mm^2]
Non-porous	n0	–	142±19	6±1	7±1	24.7±0.6	824±37	1476±185
	n20	–	179±16	6±1	3±1	16.8±0.8	507±32	585±67
	n40	–	243±14	7±1	3±1	13.5±0.3	430±22	589±83
Porous	n0	71	0.06±0.03	0.26±0.09	5±2	1.0±0.2	57±9	34±12
	n20	70	0.21±0.08	0.28±0.11	2±1	0.9±0.2	34±3	26±7
	n40	74	0.26±0.06	0.18±0.08	4±1	0.7±0.3	35±3	19±6

It is clear from the table that porosity has a very large effect on the mechanical properties of the composites. Compared to the analogous non-porous materials, the *E* modulus, tensile yield strength, tensile strength at break, elongation at break, and toughness were significantly lower. Nevertheless, here, too, the ceramic component has an important effect on mechanical properties, increasing the elasticity modulus and decreasing tensile yield stress, elongation at break and toughness.

Both the non-porous and the porous films had more than adequate mechanical properties and could be handled with ease. This indicates that these PCL-*b*-PTMC-*b*-PCL composite materials will be useful materials for the preparation of medical implants.

3.3. 3D printing of PCL-*b*-PTMC-*b*-PCL and nAp composites

The dissolution/dispersion of the PCL-*b*-PTMC-*b*-PCL and nAp composite in a crystallizable solvent, such as ethylene carbonate, should facilitate the extrusion of the composite during the 3D printing process and allow for rapid solidification of the printed structure after extrusion.

DSC analysis of the composite PCL-*b*-PTMC-*b*-PCL and nAp solutions in EC, once again indicated the presence of phase-separated block copolymers. After cooling to –100 °C, all crystallized composite solutions showed the presence of two glass transition temperatures in the second heating scan: one around –60 °C (T_{g1}) corresponding to the PCL segment of the block copolymer and one close to –20 °C (T_{g2}) corresponding to the PTMC segment of the triblock copolymer. No melting temperature corresponding to the PCL segment (which should be close to 55 °C) was observed. However, a melting temperature close to the melting point of ethylene carbonate (EC melting point is 37 °C) was seen. The observed melting temperatures were similar, with determined values of respectively 38, 39, and 36 °C for the n0, n20, and n40 composite solutions. These low melting temperatures are advantageous for the printing of the composites. Under the applied conditions, the DSC analyses showed that the n0, n20, and n40 composite solutions in EC crystallized at temperatures of respectively –9, –2, and 0 °C. Apparently, nAp has a positive effect on the crystallization rate of the EC solvent. In optimizing the 3D printing conditions, we found that cooling the printing stage with dry ice was a very convenient way to reach these temperatures and allow rapid solidification of the extruded structure.

All PCL-*b*-PTMC-*b*-PCL and nAp composite compositions could readily be printed. The n20 composite formulation in EC (25 wt% solids in 75 wt% EC) was printed at a cylinder temperature of 68 °C, an extrusion nozzle temperature of 70 °Cand an extrusion pressure of 620 kPa. Figures 4a and 4b show optical light microscopy images of the printed structures before extraction of the crystallized solvent. It can be seen that the printed structure very closely resembles the design. The composite fibres clearly do not sag, and the printed structures maintain their form stability upon 3D printing.

Figures 4c and 4d show optical microscopy images of printed structures after solvent extraction. Here too, the shape fidelity of the built structures, as compared with the design, remains very high. Apparently, in this process, the extraction of the crystallized EC solvent with water does not have a detrimental effect on the form stability of the 3D-printed structures. After a period of several weeks at ambient conditions, the printed and extracted structures were found to have kept their shape.

Figure 5 shows SEM images of the 3D-printed composite structures after extraction of the crystallized solvent and drying. Figures 5a and 5b show that under the applied printing and cooling conditions, the extruded fibres were very regular with a constant thickness and homogeneously porous as well. It can also be seen that they were well-bound to each other. From Figure 5c, the diameter of the extruded fibres could be determined to be 170 to 200 μm, indicating that the fibre diameters closely match the diameter of the extrusion nozzle and that die swell upon extrusion of the composite through the 200 μm nozzle is avoided.

The high-resolution SEM image in Figure 5d shows the presence of the needle-like nAp particles in the polymer matrix of printed structures. The regular dispersal of the nanoparticles in the (sub) micrometer-sized pores shows that during the whole process, *i.e.* upon sonication in $CHCl_3$, precipitation in methanol, redissolution in EC, printing, crystallization of the composite solution and extraction, the nAp remains homogeneously distributed in the polymer and does not significantly aggregate.

Figures 5e and 5f represent images of the characteristic pore structure that results from the crystallization and subsequent extraction with water of EC.

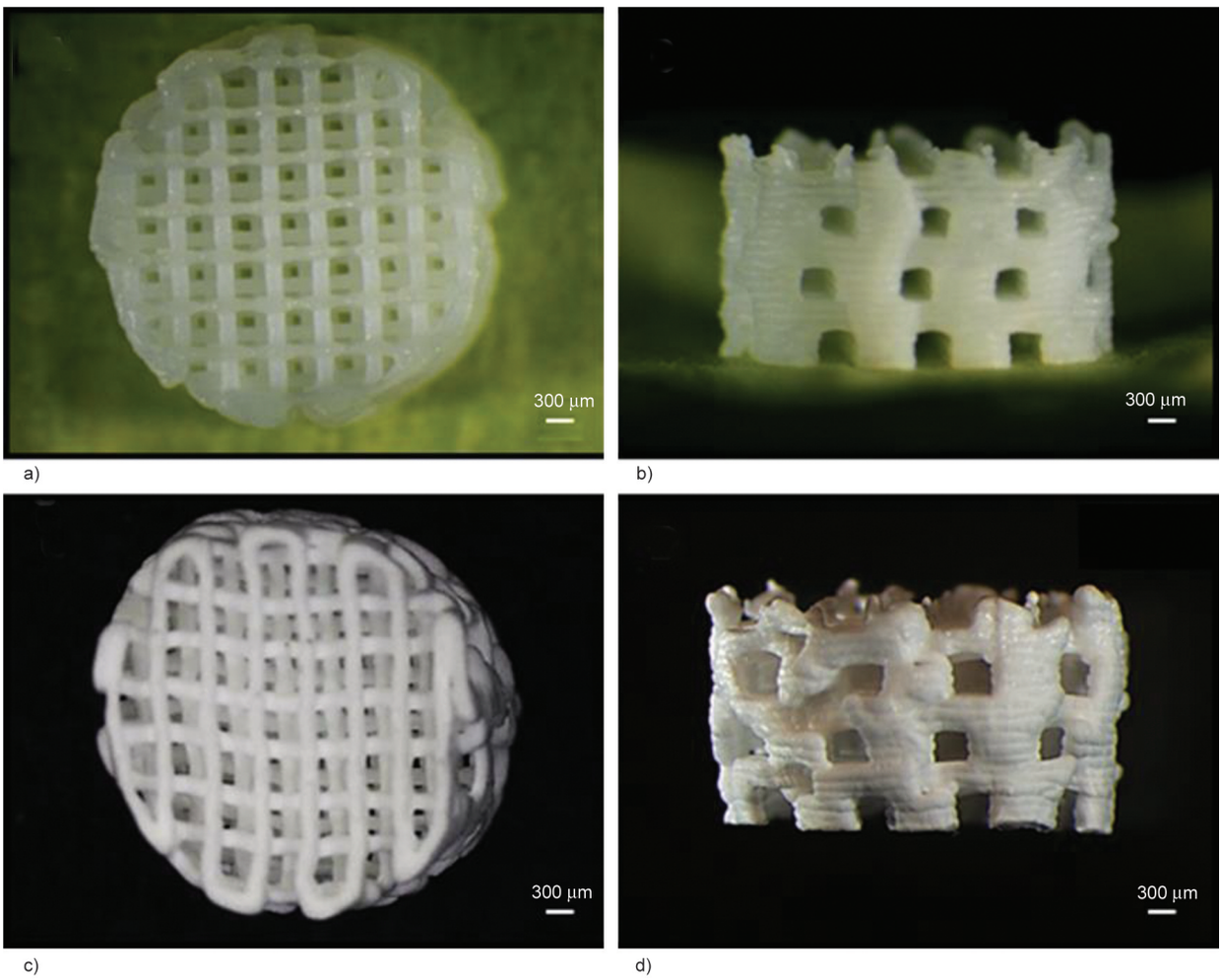

Figure 4. Optical light microscopy images of porous structures prepared by 3D printing of n20 PCL-*b*-PTMC-*b*-PCL and nAp composites from 25% solutions in ethylene carbonate. The images were obtained before extracting the crystallized solvent (a, b) and after extracting the solvent and drying (c, d).

Figure 5f highlights internal features with nanopores present. Together these images show that the 3D printed composite structures display a multiplicity in pore sizes: besides the designed and printed pore structure (with pore sizes ranging in size from 530 to 620 µm), also smaller pores (5–30 µm due to EC crystallization and even smaller ones (200–500 nm due to liquid-liquid exchange upon extraction of the solvent in the polymer-rich phase), can be discerned.

4. Conclusions

Novel biodegradable composite materials based on thermoplastic PCL-*b*-PTMC-*b*-PCL triblock copolymers and nano-sized apatite were prepared and evaluated with regard to their physical properties. Flexible materials with nAp contents of up to 35 wt% were prepared. While elasticity modulus values increased with nAp content, tensile stress, elongation at break and toughness decreased. Nevertheless, materials with excellent handling characteristics were obtained.

Porous composite structures could be prepared using ethylene carbonate as a solvent. After cooling of this low melting solvent, the solidified solvent can be extracted with water, leaving behind well-defined porous structures.

The PCL-*b*-PTMC-*b*-PCL triblock and nAp composites dissolved/dispersed in ethylene carbonate, could also be readily processed by an extrusion-based additive manufacturing processing (3D printing) operating under relatively mild conditions. Upon extraction and drying of the 3D printed structures, porous composites with pores in accordance with the design of the printed structure, and micrometer- and sub-micrometer-sized pores resulting from ethylene carbonate solvent crystallization and extraction were obtained.

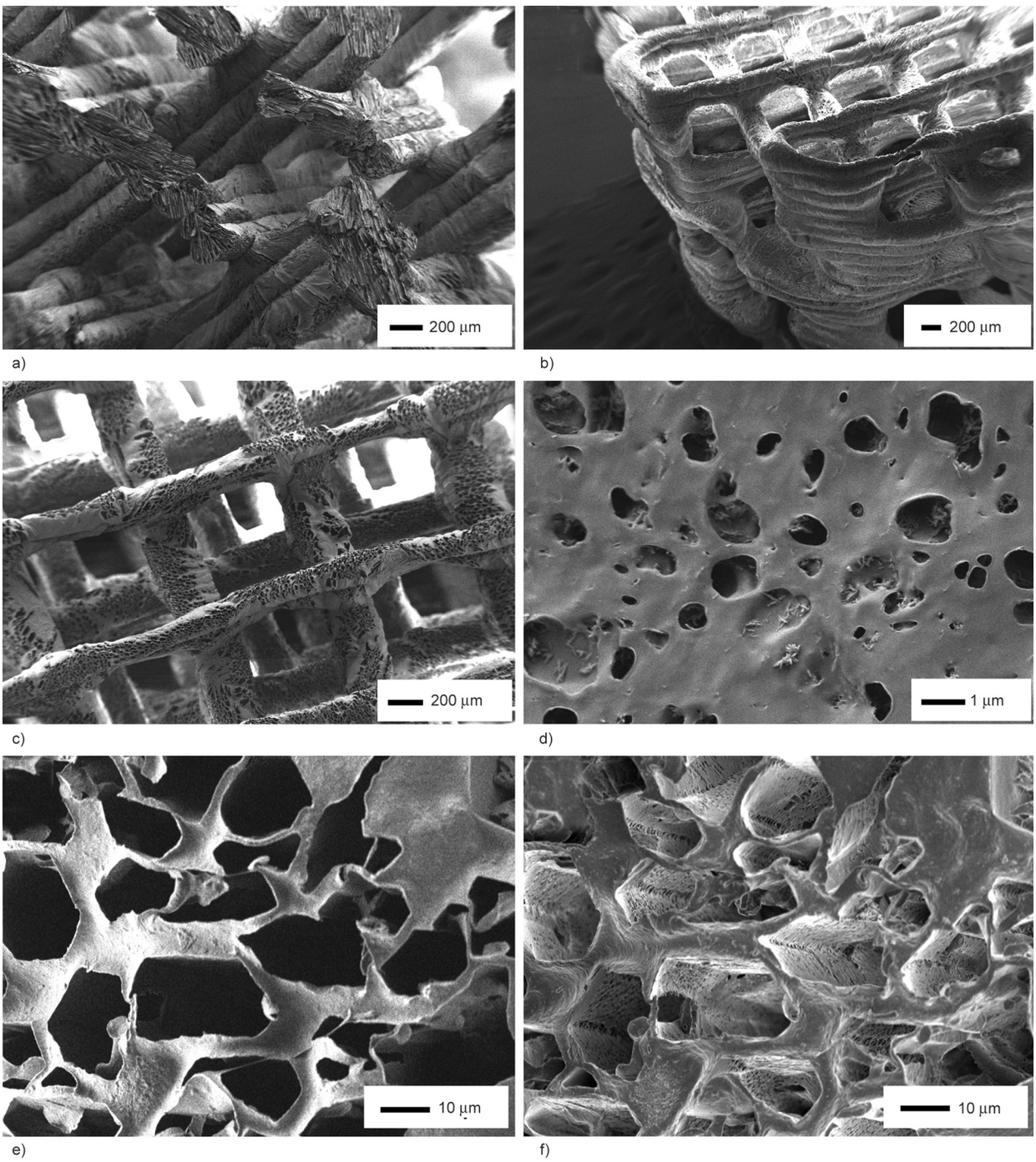

Figure 5. Scanning electron microscopy images of 3D printed porous structures prepared from 25% solutions of n20 PCL-*b*-PTMC-*b*-PCL and nAp composites in ethylene carbonate at different magnifications. The images were taken after extraction of the crystallized solvent and drying. In a)–c) the constant thickness of the extruded fibres and the homogeneity of the pores in is illustrated. Well-bound fibers (a) accurately resembling the design (b) with regular thickness matching the diameter of the extrusion nozzle (c) are shown. In d), the presence of needle-like nAp within the polymer matrix can be observed.
In e) and f), the characteristic pore structure resulting from ethylene carbonate crystallization and subsequent extraction is shown. f) Illustrates the presence of nano-sized pores.

It is expected that these biodegradable 3D-printed thermoplastic elastomeric composite structures will be of great value in bone tissue engineering. Further research in this direction will, however be required.

Acknowledgements

We would like to acknowledge Stichting Bevordering Biomaterialen for supporting AG, and the Erasmus Mundus program of the European Union for supporting LK. We would also like to thank Guner Orhan, Umut Inal, Robert Beltman and Henk Waayer for their technical assistance.

References

[1] Vidal L., Kampleitner C., Brennan M., Hoornaert A., Layrolle P.: Reconstruction of large skeletal defects: Current clinical therapeutic strategies and future directions using 3D printing. Frontiers in Bioengineering and Biotechnolology, **8**, 61 (2020). https://doi.org/10.3389/fbioe.2020.00061

[2] Hollister S. J.: Porous scaffold design for tissue engineering. Nature Materials, **4**, 518–524 (2005). https://doi.org/10.1038/nmat1421

[3] Jain R. K., Au P., Tam J., Duda D. G., Fukumura D.: Engineering vascularized tissue. Nature Biotechnology, **23**, 821–823 (2005). https://doi.org/10.1038/nbt0705-821

[4] Yang G., Mahadik B., Choi J. Y., Fisher J. P.: Vascularization in tissue engineering: Fundamentals and state-of-art. Progress in Biomedical Engineering, **2**, 012002 (2020). https://doi.org/10.1088/2516-1091/ab5637

[5] Ghilan A., Chiriac A. P., Nita L. E., Rusu A. G., Neamtu I., Chiriac V. M.: Trends in 3D printing processes for biomedical field: Opportunities and challenges. Journal of Polymers and the Enivironment, **28**, 1345–1367 (2020). https://doi.org/10.1007/s10924-020-01722-x

[6] Stansbury J. W., Idacavage M. J.: 3D printing with polymers: Challenges among expanding options and opportunities. Dental Materials, **32**, 54–64 (2016). https://doi.org/10.1016/j.dental.2015.09.018

[7] Weiner S., Wagner H. D.: The material bone: Structure-mechanical function relations. Annual Review of Materials Science, **28**, 271–298 (1998). https://doi.org/10.1146/annurev.matsci.28.1.271

[8] Lee S., Porter M., Wasko S., Lau G., Chen P-Y., Novitskaya E. E., Tomsia A. P., Almutairi A., Meyers M. A., McKittrick J.: Potential bone replacement materials prepared by two methods. MRS Online Proceedings Library, **1418**, 177–188 (2012). https://doi.org/10.1557/opl.2012.671

[9] Downey P. A., Siegel M. I.: Bone biology and the clinical implications for osteoporosis. Physical Therapy, **86**, 77–91 (2006). https://doi.org/10.1093/ptj/86.1.77

[10] Florencio-Silva R., da Silva Sasso G. R., Sasso-Cerri E., Simões M. J., Cerri P. S.: Biology of bone tissue: Structure, function, and factors that influence bone cells. BioMed Research International, **2015**, 421746 (2015). https://doi.org/10.1155/2015/421746

[11] Whang K., Healy K. E., Elenz D. R., Nam E. K., Tsai D. C., Thomas C. H., Nuber G. W., Glorieux F. H., Travers R., Sprague S. M.: Engineering bone regeneration with bioabsorbable scaffolds with novel microarchitecture. Tissue Engineering, **5**, 35–51 (1999). https://doi.org/10.1089/ten.1999.5.35

[12] Hutmacher D. W.: Scaffolds in tissue engineering bone and cartilage. Biomaterials, **21**, 2529–2543 (2000). https://doi.org/10.1016/S0142-9612(00)00121-6

[13] Madrid A. P. M., Paola A., Vrech S. M., Sanchez M. A.: Advances in additive manufacturing for bone tissue engineering scaffolds. Materials Science and Engineering, **100**, 631–644 (2019). https://doi.org/10.1016/j.msec.2019.03.037

[14] Karageorgiou V., Kaplan D.: Porosity of 3D biomaterial scaffolds and osteogenesis. Biomaterials, **26**, 5474–5491 (2005). https://doi.org/10.1016/j.biomaterials.2005.02.002

[15] Yu D., Li Q., Mu X., Chang T., Xiong Z.: Bone regeneration of critical calvarial defect in goat model by PLGA/TCP/rhBMP-2 scaffolds prepared by low-temperature rapid-prototyping technology. International Journal of Oral and Maxillofacial Surgery, **37**, 929–934 (2008). https://doi.org/10.1016/j.ijom.2008.07.012

[16] Guarino V., Gloria A., Raucci M. G., de Santis R., Ambrosio L.: Bio-inspired composite and cell-instructive platforms for bone regeneration. International Materials Reviews, **57**, 256–275 (2012). https://doi.org/10.1179/0950660812Z.00000000021

[17] Geven M. A., Sprecher C., Guillaume O., Eglin D., Grijpma D. W.: Micro-porous composite scaffolds of photo-crosslinked poly(trimethylene carbonate) and nano-hydroxyapatite prepared by low-temperature extrusion-based additive manufacturing. Polymers for Advanced Technologies, **28**, 1226-1232 (2017). https://doi.org/10.1002/pat.3890

[18] van Leeuwen A. C., Yuan H., Passanisi G., van der Meer J. W., de Bruijn J. D., van Kooten T. G., Grijpma D. W., Bos R. R. M.: Poly(trimethylene carbonate) and biphasic calcium phosphate composites for orbital floor reconstruction: A feasibility study in sheep. European Cells and Materials, **27**, 81–97 (2014). https://doi.org/10.22203/eCM.v027a07

[19] Zeng N., van Leeuwen A. C., Grijpma D. W., Bos R. R. M., Kuijer R.: Poly(trimethylene carbonate)-based composite materials for reconstruction of critical-sized cranial bone defects in sheep. Journal of Cranio-Maxillofacial Surgery, **45**, 338–346 (2017). https://doi.org/10.1016/j.jcms.2016.12.008

[20] Güney A., Malda J., Dhert W. J. A., Grijpma D. W.: Triblock copolymers based on ε-caprolactone and trimethylene carbonate for the 3D printing of tissue engineering scaffolds. The International Journal of Artificial Organs, **40**, 176–184 (2017). https://doi.org/10.5301/ijao.5000543

[21] Abràmoff M. D., Magalhães P. J., Ram S. J.: Image processing with ImageJ. Biophotonics International, **11**, 36–42 (2004).

[22] Rho J-Y., Kuhn-Sperling L., Zioupos P.: Mechanical properties and the hierarchical structure of bone. Medical Engineering and Physics, **20**, 92–102 (1998). https://doi.org/10.1016/S1350-4533(98)00007-1

[23] Wei G., Ma P. X.: Structure and properties of nano-hydroxyapatite/polymer composite scaffolds for bone tissue engineering. Biomaterials, **25**, 4749–4757 (2004). https://doi.org/10.1016/j.biomaterials.2003.12.005

[24] Lowe B., Hardy J. G., Walsh L. J.: Optimizing nanohydroxyapatite nanocomposites for bone tissue engineering ACS Omega, **5**, 1–9 (2020). https://doi.org/10.1021/acsomega.9b02917

[25] Barbieri D., Renard A. J. S., de Bruijn J. D., Yuan H.: Heterotopic bone formation by nano–apatite containing poly(D,L–lactide) composites. European Cells and Materials, **19**, 252–261 (2010). https://doi.org/10.22203/eCM.v019a24